

Detecting charge transfer at defects in 2D materials with electron ptychography

Christoph Hofer,¹ Jacob Madsen,² Toma Susi,² and Timothy J. Pennycook¹

¹*EMAT, University of Antwerp, Belgium*

²*University of Vienna, Faculty of Physics, Boltzmanngasse 5, 1090 Vienna, Austria*

Charge transfer between atoms is fundamental to chemical bonding but has remained very challenging to detect directly in real space. Atomic-resolution imaging of charge density is not sufficient by itself, as the change in the density due to bonding is very subtle compared to the total local charge density. Sufficiently high sensitivity, precision and accuracy are required, which we demonstrate here for the detection of charge transfer at defects in two-dimensional WS₂ via high-speed electron ptychography and its ability to correct errors due to residual lens aberrations.

Chemical bonding makes a material with collective properties out of an ensemble of independent atoms. As a central tenet of density functional theory (DFT) [1, 2], these properties can be entirely derived from the electron charge density. As such, measuring the charge density is of great interest, especially its variation from neutral independent atoms due to bonding. Electron diffraction and X-ray scattering can detect charge transfer [3–6], but both probe an average over a large area rather than individual atoms or atomic columns. For imaging atomic structures, electron microscopy has become an indispensable tool, and in recent years, scanning transmission electron microscopy (STEM) the de facto standard due to the simplicity of interpreting its annular dark-field (ADF) atomic-number contrast [7]. However, ADF is not sensitive to the electron charge distribution, as its contrast results from Rutherford scattering from the nuclear cores. The inelastic scattering processes detected by electron energy-loss spectroscopy (EELS) contain information about the local electronic environment [8, 9], but require high electron irradiation doses as well as the use of especially demanding first-principles spectrum simulations to interpret its fine structure [8].

Phase-contrast imaging methods, on the other hand, are known for being highly dose efficient, and indeed, local atomic-scale detection of charge redistribution due to bonding has been demonstrated in high-resolution transmission electron microscopy (HRTEM) for both single-layer hexagonal boron nitride and doped graphene [10]. However, revealing the charge redistribution in HRTEM required careful use of specific contrast transfer function (CTF) conditions with large defocus values, significantly degrading image resolution. Furthermore, due to the oscillatory CTFs of HRTEM, it is often difficult to interpret even for structural imaging, let alone disentangling charge transfer from that of the atomic structure. Fortunately, STEM phase-contrast imaging has improved greatly in the past decade. Multiple phase-imaging modes can be performed without the need for aberrations and in parallel with *Z*-contrast ADF, providing easily interpretable images of structures at the maximum resolution of the microscope. Atomic-resolution charge-density imaging has been performed with differential phase contrast (DPC), scattering center of mass (CoM) [11] and off-axis holography [12], but these tech-

niques have not been sufficient to detect charge transfer due to bonding.

Here we employ high-speed [13] focused-probe single-sideband (SSB) electron ptychography with post-collection aberration correction [14] to provide the necessary precision and accuracy to detect charge transfer directly in WS₂, including at individual point defects. In addition to the high-speed and dose-efficiency of our method allowing us to outrun damage, the ptychographic aberration correction overcomes the problem of residual aberrations that has so far prevented CoM-based methods from achieving valence imaging [15]. Accounting for residual aberrations, as we do here, is essential because they can completely obscure the effect of charge transfer, and if ignored may result in an entirely incorrect interpretation. Also crucial is the use of our new parameter-based quantification method [16] that explicitly accounts for the CTF of the imaging modality and overcomes artefacts due to the sample configuration such as mistilt.

The problem of residual aberrations is illustrated in Fig. 1 with experimental data of WS₂ from a modern aberration-corrected STEM (see Methods in Supplemental Material). Aberrations are particularly problematic when quantifying phase images [17]. Two SSB images from the same dataset are shown, one with ptychographic aberration correction and one without. Although both were acquired using the electron-optical aberration corrector, the lattice polarity in the SSB image without the additional ptychographic post-collection correction is reversed because of the residual aberrations. With such a large effect on the phase from relatively small aberrations, interpreting phase images from either ptychography or CoM-based methods, including DPC, is fraught with danger, and reliably doing so in terms of the subtle effects of charge transfer is essentially untenable.

For very thin specimens, such as 2D materials, without aberrations the phase should be flat in the double-disk overlaps in probe reciprocal space, a pair of which is shown for each SSB image in Fig. 1. This is clearly not the case without ptychographic aberration correction. We use singular value decomposition (SVD) to identify the aberrations present and counteract the phases of these aberrations, resulting in a nearly flat phase in the double-overlap regions, confirming the removal of the residual aberrations [14].

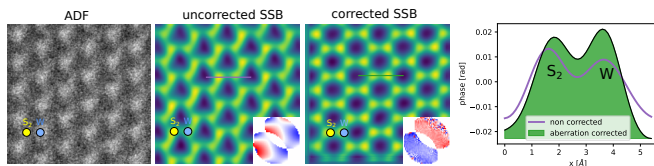


FIG. 1. **Post-acquisition aberration-corrected single-sideband (SSB) reconstruction.** a) Low-dose ADF image of WS_2 . b) SSB reconstruction of the same scan with slight residual aberrations. c) Aberration-corrected SSB reconstruction. d) Line profile showing a reversal of the sublattice contrast between b and c.

To understand the role of charge transfer in the observed contrast, we employ first-principles DFT calculations and SSB ptychography image simulations based on both DFT and independent atom model (IAM) potentials. 4D-STEM datasets were simulated using the multislice algorithm with the *abTEM* code [18], with probe parameters and sampling set to match our experimental conditions (see Methods). The results show that the contrast between the sublattice sites depends on the convergence angle of the incoming probe. For the 20 mrad convergence angle used in Fig. 1, the IAM-based S_2 phases are higher than those of the W sites. However, once bonding is included by using a scattering potential simulated with DFT, the contrast reverses, with the W sites having higher phase than the S_2 sites. This is exactly what is seen in Fig. 1c once post-collection aberration correction is applied to the experimental ptychographic image.

To quantify the influence of charge redistribution from the ptychographic images, we need to assign a phase to each of the atomic sites. Various approaches have been established for quantifying the atomic intensities of ADF images, including local maxima [7], the integration of Voronoi cells [19], Gaussian fits [20, 21], as well as template matching [22]. However, these methods do not work well for ptychography since its CTF induces a stronger nonlinear dependence on the local atomic environment [16]: neighbouring atoms can actually decrease the phase at a lattice site, which is very different to the additive behavior of probe tails in ADF imaging. This introduces a strong dependence not only on the neighboring atoms but also on sample tilt, which must be accounted for to correctly quantify such phase images. Notably, this behavior also occurs when CoM- or DPC-based images are high-pass filtered, as they often are.

We recently developed a quantification method that accounts for the contrast transfer function of these methods and is robust to both sample tilt and source size [16]. This is important here because mistilt is particularly difficult to eliminate in 2D materials and can cause significant errors in quantification, in addition to residual aberrations. With this method, the quantified phase of an atomic column is independent of both the proximity and type of the neighboring columns.

Detecting charge transfer requires that the precision of the phase measurement is better than the difference caused by the transfer, which is far more challenging than simply mapping the charge density. However, due to its effect on screening the nucleus, charge transfer can result in an order of magnitude larger change in the phase than in the potential itself (SFig. 2,3), substantially aiding its detection. Experimentally, sufficient precision is either achieved with high doses, combining measurements from multiple identical atomic sites, or both. As the dose is limited by the specimen stability, averaging over multiple sites is often unavoidable. Based on simulated estimates of the dose-dependent precision of the phase extraction of charge transfer due to bonding for WS_2 (SFig. 5), we estimate doses of $5 \times 10^4 \text{ e}^- \text{ \AA}^{-2}$ and above to be sufficient when averaging over three pairs of sites.

Fig. 2 compares experimental and simulated SSB ptychography of pristine WS_2 at a dose of $1 \times 10^5 \text{ e}^- \text{ \AA}^{-2}$. Line profiles taken across the W and S_2 sites are shown in Fig. 2b. The experimental line trace is an average of 15 pairs of sites, which at this dose should produce a very high statistical significance. Including bonding via DFT clearly alters the relative phases of the two sublattices in comparison to the IAM simulation. The DFT potential is decreased at the S_2 sites compared to the IAM because of the additional screening from the transfer of the 1.36 electrons from the tungsten atoms to the neighboring sulfur atoms; this increase in negative charge increases the screening of the positively charged nuclei at the sulfur sites, resulting in a lower overall positive potential and a reduced phase in ptychographic imaging. As can be seen, the experimental line trace matches the DFT simulation with bonding very well indeed, and is not compatible with the neglect of bonding in the IAM result.

Fig. 2d shows that the ratio of the phases of the sites that in Fig. 2c are quantified for 20 mrad depends on the probe convergence angle. This is because the convergence angle determines the strength at which different spatial frequencies are transferred in the SSB method [23, 24], which in turn determines the relative strengths at which the features of the charge density distribution appear in the phase images. However, the fact that we can see these clear differences demonstrates that the frequencies transferred by these conditions do contain information on the charge transfer induced by bonding. We emphasize that such conditions are all in the range typical for high-resolution STEM imaging. This is in contrast to conventional HRTEM, where the imaging conditions relevant to detecting charge transfer are generally not those desired for imaging the structure itself. Including atomic vibrations using thermal diffuse scattering (TDS, see Methods) slightly decreases the S_2 to W ratio compared to neglecting it, and the experimental uncertainty, estimated from the statistical site-by-site phase variation dominated by the limited signal, overlaps both values with bonding included.

The simplest defect in transition metal dichalcogenides is a chalcogen vacancy. For WS_2 this can be realized

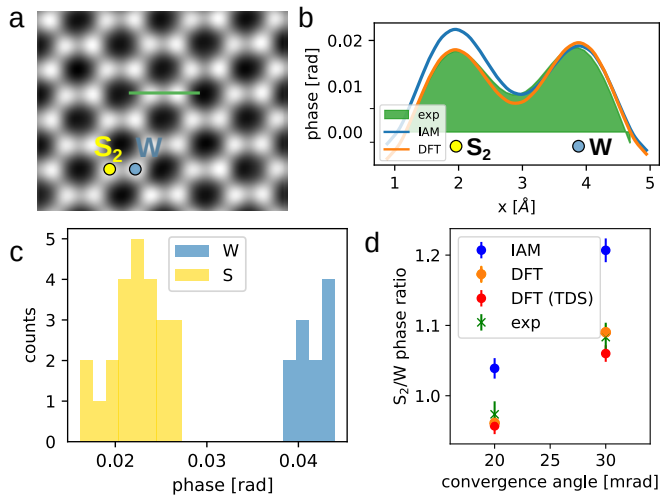


FIG. 2. **Charge-transfer measurement in WS_2 .** a) Experimental SSB image using a convergence angle of 20 mrad. b) Comparison of line profiles of SSB simulations using DFT and IAM potentials and the experimental image. c) Histogram of deconvolved S and W phases of the 20 mrad experimental SSB image. d) Ratio of the mean values of the two sublattices as a function of convergence angle using IAM and DFT potentials with and without the effect of thermal diffuse scattering (TDS), compared to experimental data for 20 and 30 mrad.

by removing a single S atom, leaving both a S vacancy and one remaining S atom at the former S_2 site (V_S). These vacancies produce a significantly reduced phase in SSB reconstructions, as shown in the DFT-based SSB images in Fig. 3a, where three S vacancy sites are distributed around the central W atom (V_{3S}). This data also showcases the ability of ptychography to reveal light atoms next to heavy elements [14, 25]: the S sites are in general not readily visible in the high-angle ADF signal under these conditions, and thus S vacancies are only discernible in the phase images (see also SFig. 6,7).

Interestingly, we observe a higher W site phase close to the S vacancies, with the intensity of the W depending on the density of the vacancies in the area. The reason for this is two-fold: firstly, the CTF of the SSB reconstruction results in a negative halo that reduces the phase of atoms close to other atomic sites. Importantly, our phase optimization method takes this into account, allowing us to detect the second effect, the charge transfer.

To systematically study the charge transfer at defects, we simulated a region of WS_2 with an increasing numbers of S vacancies using both IAM and DFT potentials. Fig. 3a shows the DFT-based SSB phase image with three monovacancies (V_{3S}). The difference between IAM- and DFT-based potentials, shown in Fig. 3b, increases at the W sites next to vacancies and further increases with the density of defects (see also SFig. 8).

This increase would be surprising if one assumes that defects reduce charge transfer due to W atoms having fewer S neighbors. If that were the case, one would see a

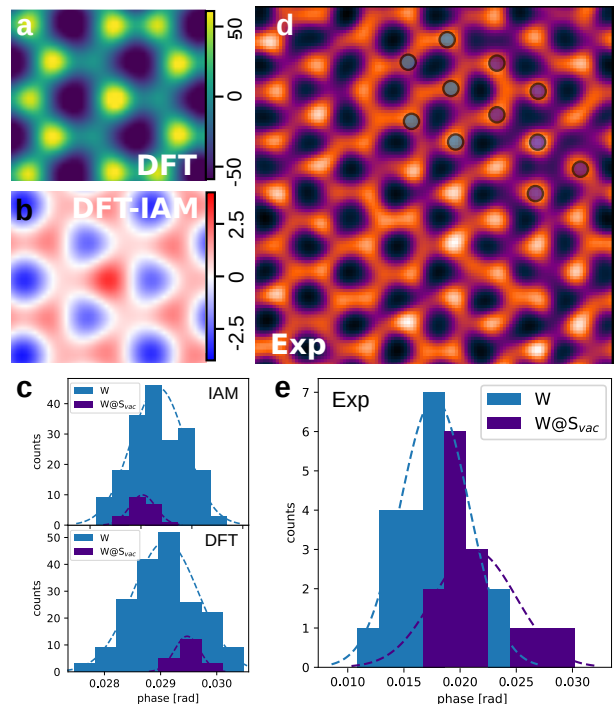


FIG. 3. **Analysis of defective WS_2 .** (a) SSB simulation of three S vacancies based on the DFT potential. (b) Difference between IAM and DFT simulations of the same structure. (c) Histogram of extracted deconvolved phases of IAM- and DFT-based simulations of a defective area similar to the experimental defect density, showing a difference between W in the pristine (blue) and the high defect-density region (dark blue) at a $1 \times 10^5 \text{ e}^-/\text{\AA}^2$ dose. The statistical distribution is based on 10 randomly noised images with this dose. (d) Experimental SSB image of defective WS_2 . The overlaid circles indicate pristine W (blue) and W close to the defects (dark blue), respectively. (e) Histogram of the deconvolved phases of pristine W (blue) and W surrounded by vacancies (dark blue) extracted from the image in (d).

smaller phase shift in the DFT-based simulations, which is not what is observed. Fig. 4 shows variation of the phase ratio of the central W site to a neighboring S vacancy site ($W@S_{vac}/S_{vac}$) with respect to the density of vacancies. In the extreme three-divacancy case (V_{3S_2}), the W atom has lost all its nearest neighbors and would therefore seem more similar to an independent atom, for which one might expect a negligible difference between DFT and IAM. However, this is not the case (see simulated SSB images and projected all-electron potentials in SFig. 7,8) and this highly defected case is in fact further from the IAM result with a higher $W@S_{vac}/S_{vac}$ ratio than the other results using the DFT potentials. The IAM results show a negligible variation between the configurations as they should. The fact that S vacancies produce occupied states at the defect sites [26, 27] does not explain the observed contrast, and additional studies have shown charge redistribution occurs towards the defect sites [28].

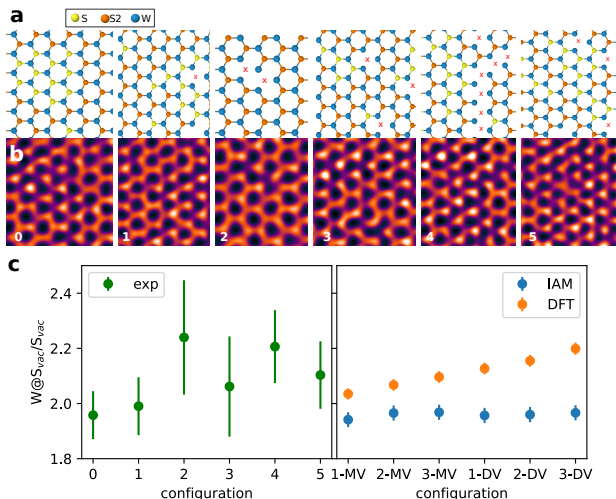


FIG. 4. **Analysis of the dependence of the W/S_{vac} phase ratio on defect density.** (a,b) Atomic models and SSB images of defective WS₂ containing different numbers of mono- and divacancies. (c) Phase ratio between W atoms next to vacancies and at S monovacancies. The variation of ratios clearly depend on the configuration type corresponding to different defect densities. Right: simulated ratios for an increasing density of defects.

To understand this phenomenon, we plot the three-dimensional (pseudo-)electron valence densities of each configuration in SFig. 9, where a different picture emerges. The line profiles over the W site close to the defects indeed show a lower density of valence electrons when increasing the number of defects, in agreement with the increase of phase we observe at this site. The electrons are redistributed towards the next W sites, which creates W-W bonding that is stronger the more S vacancies are involved in the system. Thus we need to consider longer-range charge rearrangement than merely the first nearest neighbors to understand the full picture.

The relative difference between IAM and DFT can reach up to 10% (cf. Fig. 4c), which is higher than in the pristine case and one might thus conclude that detecting charge transfer is easier at defects. However, defect configurations are often unique and complex and therefore a statistical assessment such as analysing multiple sites is very challenging with each atom potentially undergoing different amounts of charge transfer. Secondly, the dose one can use to probe defective configurations is usually lower, due to their greater propensity to damage, increasing the uncertainty per site. In this case the dose we could use before damage was only $3 \times 10^4 \text{ e}^-/\text{\AA}^2$.

To ascertain if we can detect charge transfer at defects experimentally, we used electron irradiation to obtain a variety of vacancy densities and atomic configurations in the sample. A representative area is shown in Fig. 3d (full view in SFig. 5). Fig. 3c shows the extracted phases of the W atoms in the pristine area (blue) and the W atoms close to vacancies, labeled as $W@S_{vac}$ (dark purple). Indeed, the calculated mean value for $W@S_{vac}$

shows a small but detectable shift in the DFT simulations compared to pristine W atoms. Both types of simulations were treated with Poisson noise in the 4D diffraction data corresponding to the experimental dose. Note that the shift is very small as the simulated structure only contains monovacancies (cf. SFig. 6a,b). The shift would be significantly higher if this specific area of interest also contained divacancies. This qualitative assessment also agrees with the experimental data, where the shift between $W@S_{vac}$ and W is observable in Fig. 3e.

To quantify the effect, we calculated phase ratios between the atomic sites where the charge transfer occurs. We compared the ratio of the W site to vacancy site phases, and indeed find a significant range of ratios ($W@S_{vac}/S_{vac}$ from 1.99 to 2.23) when analysing different areas in the sample. Fig. 4a and b show areas of the sample with different vacancy configurations and densities. The trend of charge transfer increasing with the amount of defects is also reflected in the experimental ratios (see Fig. 4c): Configurations 0 and 1 do not contain any divacancies and their ratios are in the lower range. Configurations 2–5 all contain divacancies and their ratios are clearly higher indicating a higher amount of charge transfer. Interestingly, configurations 2 and 4 are the only ones which contain neighboring divacancies, resulting in an even higher ratio (and charge transfer), again in agreement with the simulation analysis.

To conclude, we have experimentally detected charge transfer in monolayer WS₂ including at its defects, via the influence of the electron distribution in the material on the phase of the probe electrons using electron ptychography and our parameter-based quantification method. Post-collection aberration correction is crucial to obtain accurate phases for charge-transfer measurements, and the convergence angle is also an important parameter, as it defines which spatial frequencies are transferred. Our results indicate that the frequencies at which charge transfer is detectable conveniently include those used for atomic-resolution imaging. Simulations based on first-principles charge redistribution due to bonding lead to an excellent agreement in the pristine case. For defective areas, we observe a notable phase increase of the metal site close to chalcogen vacancy sites, which significantly increases with the number of vacancies involved, as shown both theoretically and experimentally. Our study thus presents a significant advance in detecting atomic-scale charge transfer at defects.

We acknowledge funding from the European Research Council (ERC) under the European Union’s Horizon 2020 Research and Innovation Programme via Grant Agreement No. 802123-HDEM (C.H. and T.J.P.) and No. 756277-ATMEN (J.M. and T.S), and FWO Project G013122N “Advancing 4D STEM for atomic scale structure property correlation in 2D materials” (C.H.). We further acknowledge computational resources provided by the Vienna Scientific Cluster (VSC).

-
- [1] P. Hohenberg and W. Kohn, Phys. Rev. **136**, B864 (1964).
- [2] W. Kohn and L. J. Sham, Phys. Rev. **140**, A1133 (1965).
- [3] P. Coppens and E. D. Stevens (Academic Press, 1977) pp. 1–35.
- [4] T. S. Koritsanszky and P. Coppens, Chemical Reviews **101**, 1583 (2001).
- [5] J. M. Zuo, Reports on Progress in Physics **67**, 2053 (2004).
- [6] L. Wu, Y. Zhu, and J. Taftø, Phys. Rev. B **59**, 6035 (1999).
- [7] O. L. Krivanek, M. F. Chisholm, V. Nicolosi, T. J. Pennycook, G. J. Corbin, N. Dellby, M. F. Murfitt, C. S. Own, Z. S. Szilagy, M. P. Oxley, S. T. Pantelides, and S. J. Pennycook, Nature **464**, 571 (2010).
- [8] Q. M. Ramasse, C. R. Seabourne, D.-M. Kepaptsoglou, R. Zan, U. Bangert, and A. J. Scott, Nano Letters **13**, 4989 (2013).
- [9] H. Tan, S. Turner, E. Yücelen, J. Verbeeck, and G. Van Tendeloo, Phys. Rev. Lett. **107**, 107602 (2011).
- [10] J. C. Meyer, S. Kurasch, H. J. Park, V. Skakalova, D. Künzler, A. Gross, A. Chuvilin, G. Algara-Siller, S. Roth, T. Iwasaki, U. Starke, J. H. Smet, and U. Kaiser, Nature materials **10**, 209–215 (2011).
- [11] S. Calderon V, R. V. Ferreira, D. Taneja, R. Jayanth, L. Zhou, R. M. Ribeiro, D. Akinwande, and P. J. Ferreira, Nano Letters **21**, 10157 (2021).
- [12] V. Boureau, B. Sklenard, R. McLeod, D. Ovchinnikov, D. Dumcenco, A. Kis, and D. Cooper, ACS Nano **14**, 524 (2020), <https://doi.org/10.1021/acsnano.9b06716>.
- [13] D. Jannis, C. Hofer, C. Gao, X. Xie, A. Béché, T. Pennycook, and J. Verbeeck, Ultramicroscopy **233**, 113423 (2022).
- [14] H. Yang, R. Rutte, L. Jones, M. Simson, R. Sagawa, H. Ryll, M. Huth, T. Pennycook, M. Green, H. Soltau, Y. Kondo, B. Davis, and P. Nellist, Nature Communications **7**, 12532 (2016).
- [15] J. Martis, S. Susarla, A. Rayabharam, C. Su, T. Paule, P. Pelz, C. Huff, X. Xu, H.-K. Li, M. Jaikissoon, V. Chen, E. Pop, K. Saraswat, A. Zettl, N. R. Aluru, R. Ramesh, P. Ercius, and A. Majumdar, “Imaging the electron charge density in monolayer mos2 at the Ångstrom scale,” (2022).
- [16] C. Hofer and T. J. Pennycook, Ultramicroscopy , 113829 (2023).
- [17] O. Lehtinen, D. Geiger, Z. Lee, M. B. Whitwick, M.-W. Chen, A. Kis, and U. Kaiser, Ultramicroscopy **151**, 130 – 135 (2015).
- [18] J. Madsen and T. Susi, Open Research Europe **1** (2021), 10.12688/openreseurope.13015.2.
- [19] H. E, K. MacArthur, T. Pennycook, E. Okunishi, A. D’Alfonso, N. Lugg, L. Allen, and P. Nellist, Ultramicroscopy **133**, 109 – 119 (2013).
- [20] S. Van Aert, J. Verbeeck, R. Erni, S. Bals, M. Luysberg, D. V. Dyck, and G. V. Tendeloo, Ultramicroscopy **109**, 1236 – 1244 (2009).
- [21] A. De Backer, K. van den Bos, W. Van den Broek, J. Sijbers, and S. Van Aert, Ultramicroscopy **171**, 104 – 116 (2016).
- [22] C. Hofer, V. Skákalová, J. Haas, X. Wang, K. Braun, R. S. Pennington, and J. C. Meyer, Ultramicroscopy **227**, 113292 (2021).
- [23] H. Yang, T. J. Pennycook, and P. D. Nellist, Ultramicroscopy **151**, 232 (2015).
- [24] C. M. O’Leary, G. T. Martinez, E. Liberti, M. J. Humphry, A. I. Kirkland, and P. D. Nellist, Ultramicroscopy **221**, 113189 (2021).
- [25] C. Gao, C. Hofer, D. Jannis, A. Béché, J. Verbeeck, and T. J. Pennycook, Applied Physics Letters **121**, 081906 (2022), <https://doi.org/10.1063/5.0101895>.
- [26] B. Schuler, D. Y. Qiu, S. Refaely-Abramson, C. Kastl, C. T. Chen, S. Barja, R. J. Koch, D. F. Ogletree, S. Aloni, A. M. Schwartzberg, J. B. Neaton, S. G. Louie, and A. Weber-Bargioni, Phys. Rev. Lett. **123**, 076801 (2019).
- [27] S. Yuan, R. Roldán, M. I. Katsnelson, and F. Guinea, Phys. Rev. B **90**, 041402 (2014).
- [28] S. Salehi and A. Saffarzadeh, Surface Science **651**, 215 (2016).
- [29] J. Enkovaara, C. Rostgaard, J. J. Mortensen, J. Chen, M. Dulak, L. Ferrighi, J. Gavnholt, C. Glinsvad, V. Haikola, H. A. Hansen, and et al., J. Phys. Condens. Matter **22**, 253202 (2010).
- [30] R. Bader, *Atoms in Molecules: A Quantum Theory* (Oxford University Press, 1990).
- [31] W. Tang, E. Sanville, and G. Henkelman, J. Phys.: Condens. Matter **21**, 084204 (2009).
- [32] T. Susi, J. Madsen, U. Ludacka, J. J. Mortensen, T. J. Pennycook, Z. Lee, J. Kotakoski, U. Kaiser, and J. C. Meyer, Ultramicroscopy **197**, 16 (2019).
- [33] I. Lobato and D. Van Dyck, Acta Crystallographica Section A **70**, 636 (2014).
- [34] C. Hofer, G. C., and T. J. Pennycook, “Pyptychostem,” <https://gitlab.com/pyptychostem/pyptychostem> (2021).

Supplemental Material A: Methods

1. Sample preparation

WS₂ was synthesized on Si/SiO₂ by physical vapor deposition from WS₂ powder. The flakes were then transferred to a Quantifoil(R) TEM grid by a drop of isopropanol. The transfer was completed by etching the SiO₂ with a KOH solution and cleaning by deionized water.

2. Transmission electron microscopy

STEM experiments were conducted on a ThermoFisher Themis Z instrument equipped with a Timepix3 camera at 60 keV. The probe convergence angle was set to 20 or 30 mrad and the beam current was ca. 2 pA. Typical 4D datasets included 1024×1024 probe positions with a dwell time of 1–5 μ s. The list of events provided by the Timepix3 was converted to 4D data using an in-house code. The detector sampling was chosen to be approx. 30–40 pixels for the bright field disk and the real-space sampling was ca. 0.1–0.15 \AA per pixel. The ADF detector semi-angular range was 70 to 220 mrad. To increase the signal-to-noise ratio, several frames (up to 10) were aligned and averaged. Typical resulting total doses were approx. $10^5 e^-/\text{\AA}^2$.

3. Density functional theory

For DFT, we used the projector-augmented wave method in the open-source package GPAW [29]. The hexagonal unit cell of WS₂ was made orthogonal, its size was optimized, and then used to create 5×3×1 supercells of WS₂ (a total of 90 atoms) with 8.9 \AA of vacuum between the periodic images of the layers (perpendicular cell size of 12 \AA). To obtain relaxed structures for the multislice simulations, the atomic positions were optimized using a plane-wave basis with a cutoff energy of 500 eV and 3×3×1 \mathbf{k} -points to sample the Brillouin zone until residual forces were below 0.02 eV/ \AA . To create models with defects, we removed one or more S atoms, and re-relaxed the atomic positions.

To verify the convergence of the computational parameters, we further relaxed selected models (pristine, 3MV, 3DV) using a higher plane-wave cutoff of 800 eV, a denser \mathbf{k} -point mesh of 5×5×1, and included spin polarization. For these DFT potentials, we ran the full 4D-STEM simulations followed by the single-sideband reconstruction and kernel optimization (see below). Differences in the phase ratios of the sites with respect to the default parameters were at most 0.5%, which we have include in the uncertainty estimates for our computational values.

Charge transfer between the W and S₂ columns was estimated via Bader partitioning [30] of the all-eletron charge density using the grid-based implementation of Henkelman and colleagues [31]. The resulting atomic charges for the pristine system were compared to those calculated for atoms surrounding the S vacancy.

4. Multislice simulations

For the multislice simulations, the DFT potential was calculated from the all-electron charge density converged with GPAW, as described previously [32]. For the IAM, the potential was taken to be a superposition of individual tabulated atomic potentials, as parametrized by Lobato [33]. A lateral real-space sampling of 0.05 \AA has been used for both potentials as well as a perpendicular slice thickness of 1.0 \AA .

Thermal diffuse scattering was included by running DFT-based velocity-Verlet molecular dynamics (MD) with a timestep of 2 fs, initialized with a Maxwell-Boltzmann temperature of 300 K and thermalized for 100 timesteps. Ten MD frozen-phonon snapshots were generated by saving the converged electron density every 50 timesteps, and datasets averaged over the ensemble. Although more images would likely be required for full convergence of an atomically thin material, the cost of DFT/MD for large supercells is high and we do not believe this affects our conclusions.

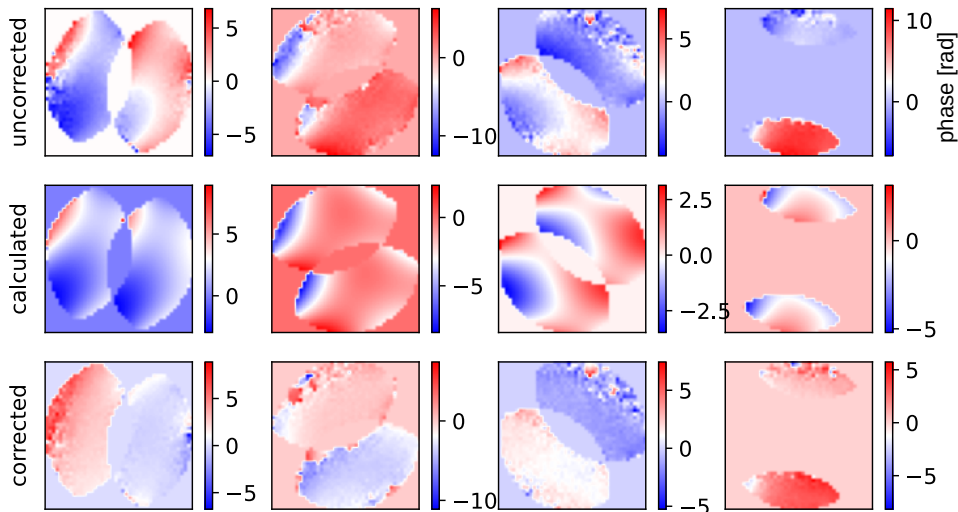
4D-STEM simulations were carried out using the multislice approach as implemented in the open-source package *abTEM* [18]. All simulation parameters were set to the experimental parameters, including the convergence angles and the dose per area simulated as Poisson noise of the diffraction patterns. To estimate statistical variation caused by the limited dose, multiple randomly noised datasets could be analyzed as indicated in the main text. The reciprocal-space sampling was 0.06 \AA^{-1} . For ADF, we note that DFT and IAM potentials produce essentially identical contrast.

5. Single-sideband ptychography

SSB ptychography was performed with the open-source PyPtychoSTEM package [34], using either the experimental or simulated 4D datasets as input. The step size was chosen to be 0.1–0.15 Å per pixel (matched in the SSB reconstruction) and the voltage was 60 kV. The convergence angle was set to 20 or 30 mrad. Post-collection aberration correction was applied using SVD to identify the residual aberrations which were then counteracted. As an example, for the case of the data shown in Fig. 1 of the main text, the SVD algorithm identified residual aberrations of $C_{10} = -8.824$ nm, $C_{12a} = 3.019$ nm, $C_{12b} = 7.824$ nm, $C_{21a} = -568.889$ nm, $C_{21b} = -731.313$ nm, $C_{23a} = 483.886$ nm, $C_{23b} = 14.429$ nm, $C_{30} = 43.45$ μm , $C_{32a} = -2.129$ μm , $C_{32b} = -15.737$ μm , $C_{34a} = -1.167$ μm , $C_{34b} = -33.608$ μm . SFig. 1 shows the uncorrected, calculated and compensated double disk-overlap phases at different frequencies in top, middle and bottom, respectively.

6. Kernel method for assigning phases to atomic sites

The phases were extracted by an optimization method where atomic phases are fitted to the target image [16]. First, an initial atomic model that represents the experimental configuration is aligned with the target image. The model is converted to a point potential, which is convoluted with a kernel calculated by the contrast transfer function of SSB. The resulting simulation is compared with the target image and their correlation is maximized by optimizing the alignment between the model and the experimental image, width of the kernel and the intensities of the point potential. For the experimental data, the sample tilt is also optimized. Correlations were above 99% for the simulated data and above 93% for the experimental data.

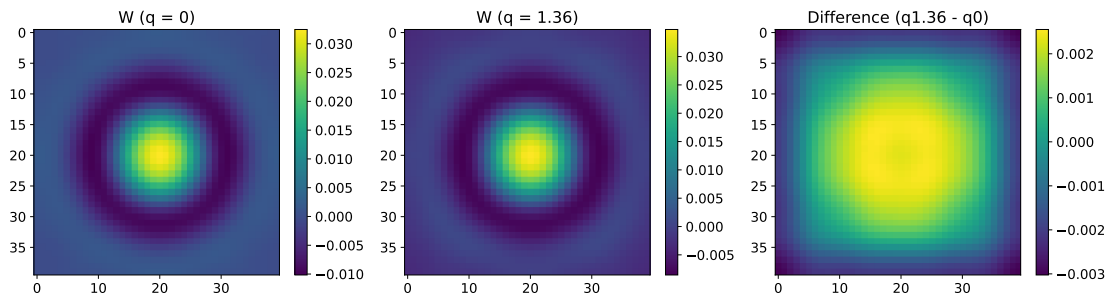


Supplemental Figure 1. **Unwrapped phases of the double-disk overlaps (DDO) at different frequencies.** Top: Uncorrected DDO phases. Middle: SVD calculated DDO phases used for the aberration correction. Bottom: Compensated DDO phases.

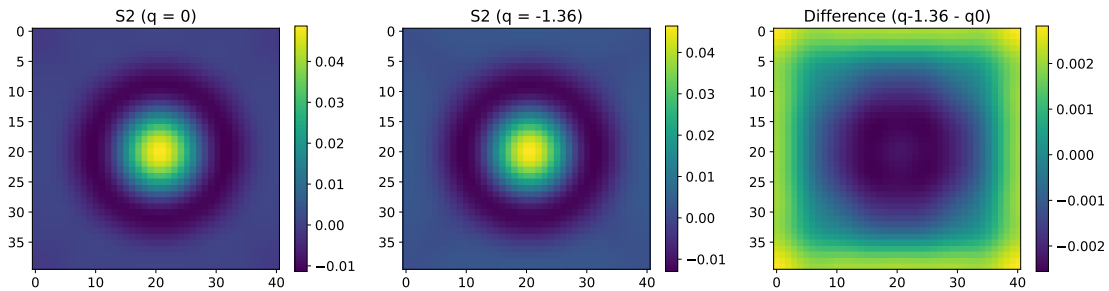
Supplemental Material B: Additional data

1. Effect of charge transfer on phase shifts

In pristine WS_2 , the less electronegative tungsten atoms donate 1.36 electrons to the neighboring sulfur atoms. Using DFT-based potentials for single W atom SSB ptychography simulations, we can study the effect of charge removal or addition on the SSB phase, shown in S Figs. 2 and 3. The left panels show an isolated W atom or S_2 column, which correspond to an IAM model. The middle panels show the phase for these models with an additional / reduced charge q equal to 1.36 elementary charges, i.e. to a removal / addition of 1.36 electrons, corresponding to the magnitude of charge transfer in WS_2 . As indicated by the difference between the two plotted in the right columns, the phase change is up to 8% for the W and -5% for S_2 . In practise, the differences are smaller as charge is not completely removed into a uniform compensating background charge as required by DFT, but rather transferred to nearby sites. This example corresponds to perfect ionicity of the chemical bond, while in practise any covalency reduces the contrast. The crucial point, however, is that due to its effect on screening the nucleus, charge transfer can result in an order of magnitude larger change in the phase than in the potential itself, which only changes by 0.5%. This larger change in the phase substantially aids the detection of charge transfer.



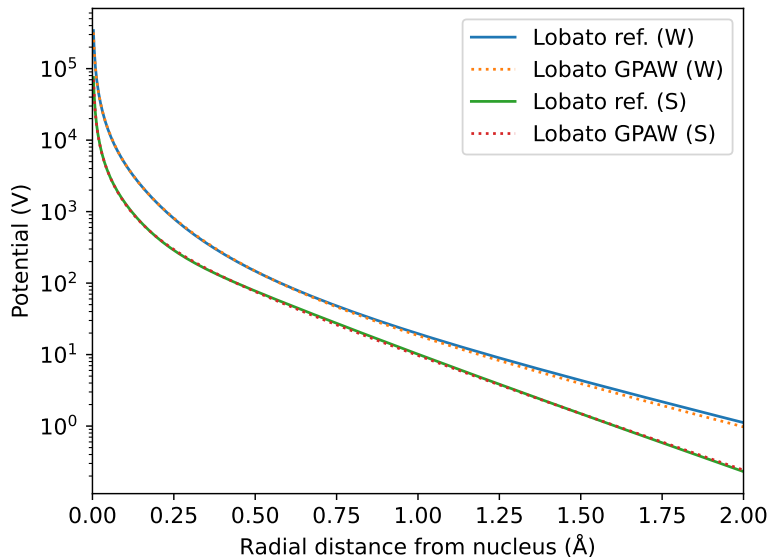
Supplemental Figure 2. **Phase change induced by charge removal.** Left: Phase image of an independent W atom. Middle: Phase image of a W atom with a removed charge of 1.36 electrons. Right: Difference between the two.



Supplemental Figure 3. **Phase change induced by charge addition.** Left: Phase image of an isolated S_2 column. Middle: Phase image of a S_2 column with an added charge of 1.36 electrons. Right: Difference between the two.

2. IAM parametrization

Another potential source of uncertainty in our analysis of the simulated phase ratios are unavoidable differences in how the IAM and DFT potentials are constructed. From GPAW, we recover the exact core-electron density from the projector augmentation functions, to which the self-consistent valence density is added alongside the nuclear contributions. An IAM such as the Lobato parametrization, on the other hand, is a fit to an atomic radial potential typically obtained from a relativistic Hartree-Fock calculation, with a limited number of fitting parameters and a specific functional form. Although care has been taken in *ab*TEM to ensure that DFT and IAM potentials are constructed in a consistent way, phase differences due to charge transfer are so small that minor numerical details might matter.



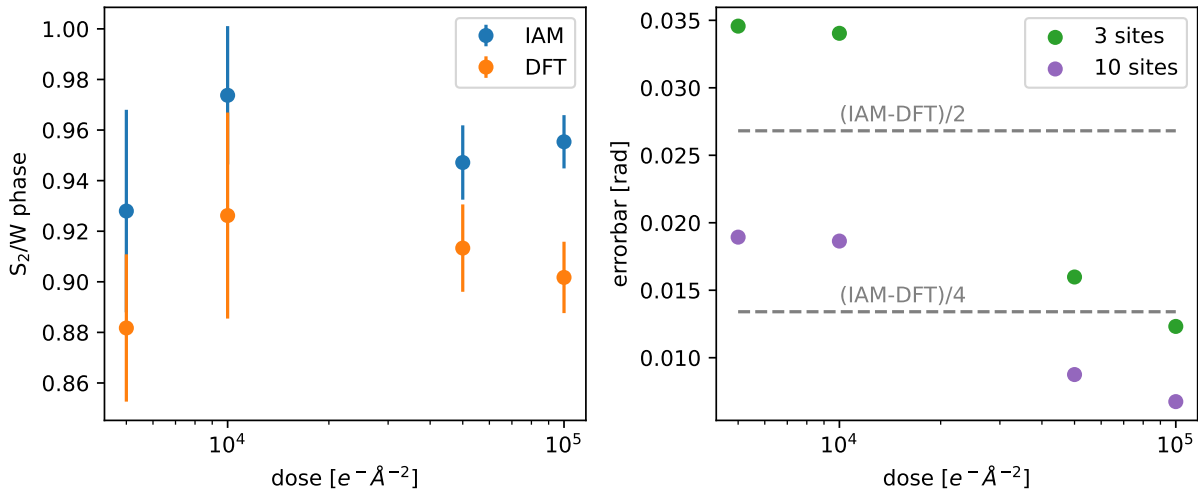
Supplemental Figure 4. **Comparing IAM parametrizations.** Radial potentials calculated for W and S atoms based on the IAM parametrization of Lobato (solid lines) compared to a custom parametrization of the same functional form fitted to an atomic GPAW calculation (dotted lines). Minor differences can be observed further away from the nuclei (note the logarithmic scale of the vertical axis).

To estimate this effect, we ran GPAW calculations for isolated neutral W and S atoms, and fitted the resulting radial potentials with the parametrization used by Lobato to create a custom IAM based on our DFT potential. SFig. 4 shows the fitted potential compared to the original Lobato parametrization, with only very minor differences further away from the nucleus. We then performed our full analysis (generation of potentials, 4D-STEM simulation, SSB reconstruction, kernel optimization) on isolated W and S_2 columns using both potentials, and found a 0.9% difference in the S_2/W phase ratio between the two parametrizations. Although our full DFT potential may arguably be more accurate, we have nonetheless included this as an uncertainty for our simulated IAM values in the main text.

3. Phase uncertainty due to limited dose

Experimentally, sufficient precision is either achieved with high doses, combining measurements from multiple identical atomic sites, or both. Dose is the most limiting factor when it comes to phase-difference measurements, thus averaging over multiple sites is often unavoidable. The amount of electron exposure of a specimen until damage occurs depends on the material and typical doses for 2D materials range from 10^4 – 10^6 $e^- \text{Å}^{-2}$. The difference between the S_2/W ratios have to be sufficiently separated so that their uncertainties are not overlapping. The error bars, which are calculated by the variation of phases due to noise, depend on the dose as well as on the number of atoms analysed. Lower statistics are desirable when the charge transfer of individual atoms are determined rather than the charge transfer in an ensemble of atoms. This is crucial when analysing defects as their configurations are often unique.

To estimate the dose-dependent precision of the phase extraction of charge transfer due to bonding for WS_2 , we show in SFig. 5 the effect on the quantified S_2/W phase ratio for the IAM and DFT potentials using first just three pairs of sites. Since a ratio is calculated in this analysis, the relative errors between both atomic sites are summed for the total relative error. The uncertainties are sufficiently small to distinguish the IAM (no bonding) and DFT (bonding) simulations for doses of 5×10^4 $e^- \text{Å}^{-2}$ and above for three measurements. The error decreases with the square root of the number of sites, \sqrt{N} . Thus for instance with 10 pairs of sites, the influence of charge transfer is significant compared to the uncertainty at doses at least as low as 5×10^3 $e^- \text{Å}^{-2}$.



Supplemental Figure 5. **Accuracy of phase extraction.** Left: Ratio between the S_2 and W site phases at different doses. The error bar is calculated by the variation of phases as a function of Poisson noise. Right: Comparison of the ratios with different numbers of sampled sites. The horizontal dashed lines denote limits precision as fractions of the difference between IAM and DFT simulations.

4. Phase shifts at defective sites

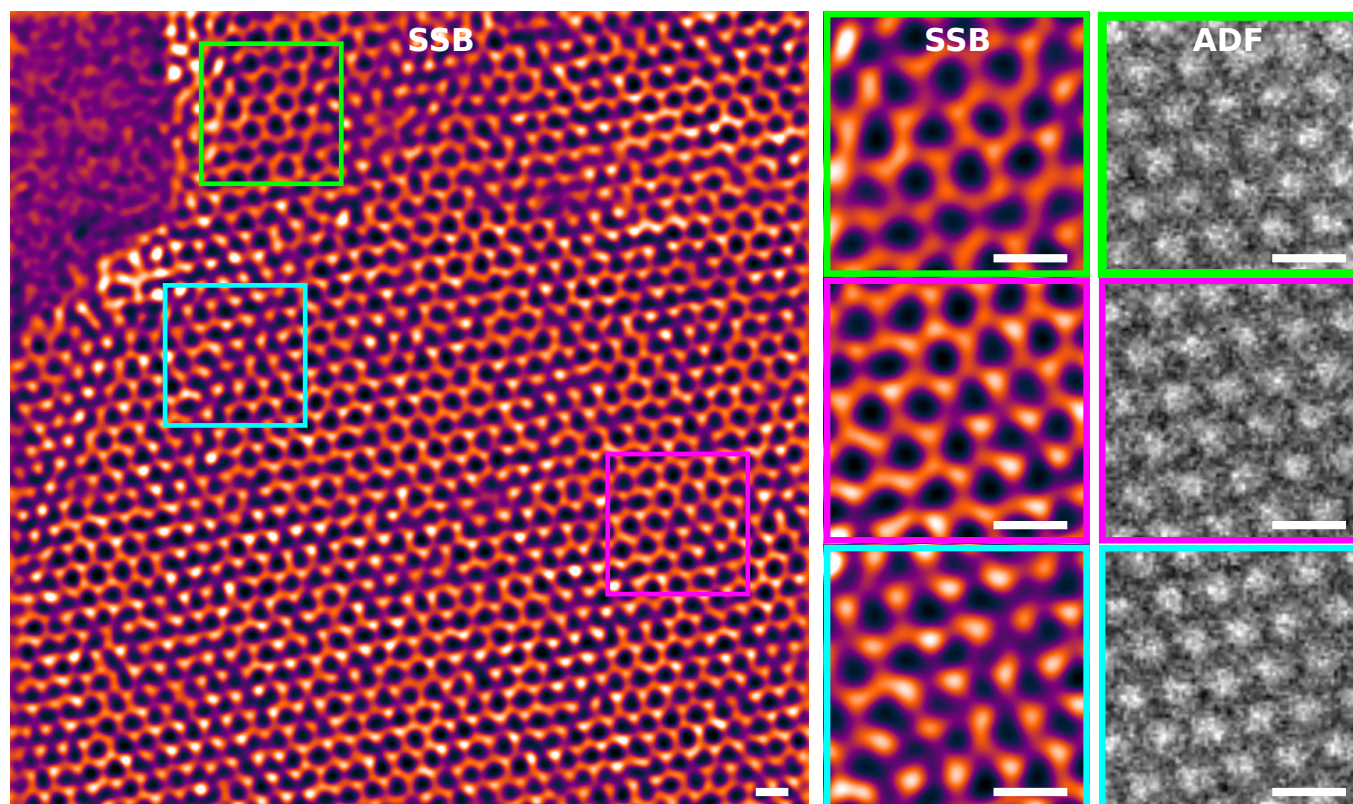
SFig. 6 shows a large area of the defective WS_2 , with smaller regions highlighted on the right side. The green box shows a small region of pristine lattice, the purple box a region with several S vacancies, and the cyan box a full line defect. In all cases, the SSB shows a much clearer image of the defects than the ADF image; it is difficult to even identify the S sites in the ADF signal. Besides this, the phase of W is also higher at sites with a higher defect density. This is due to both the contrast mechanism of SSB as well as charge transfer. All six different configurations discussed in the main text are present in this image.

SFig. 7a shows a simulation of the defective area that is used for the analysis in Fig. 3 of the main text containing several monovacancies. SFig. 7b shows another example of a small region of the experimental SSB image of a defective region. The experimental phases from all the sites in SFig. 7b are extracted and shown in the corresponding histograms on the right. For this specific region, the S vacancies, the pristine sites (S_2 and W) and the W close to the S vacancies ($W@S_{vac}$) are identified manually. As one can see, the $W@S_{vac}$ sites have a higher phase than the corresponding pristine W . This is a result of the charge transfer at the defective sites, as discussed in the main text. The magnitude of the shift is related to the amount of charge transfer.

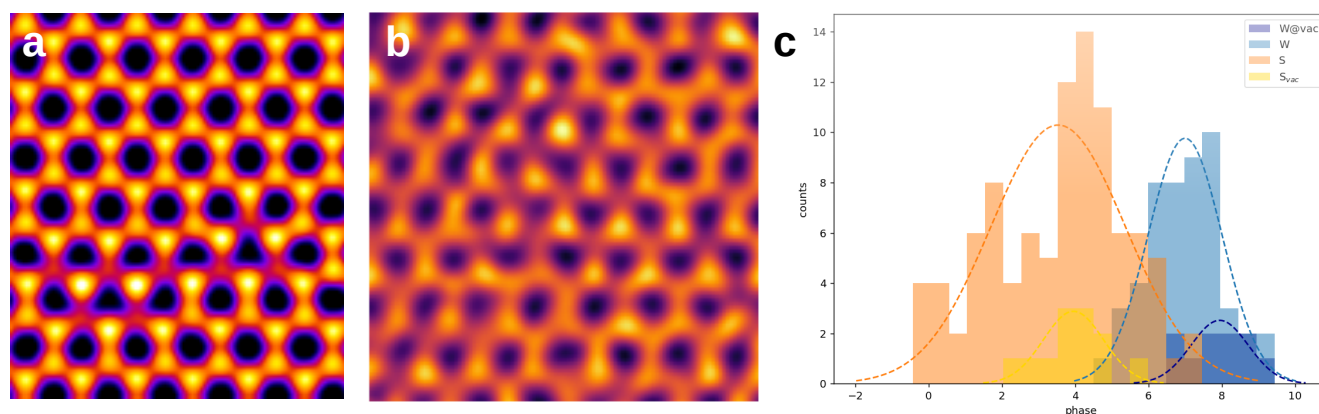
SFig. 8 further shows SSB image simulations based on the DFT and IAM potentials as well as the difference between the IAM and DFT SSB images that result from charge transfer for an increasing number of defects. The first three rows show one to three monovacancies (MVs) surrounding a W site, the last three also include divacancies (DVs). Note that the DVs are based on removing additional S atoms from the MV sites, meaning there is a systematic increase of the density of defects from left to right. The contrast is kept constant, with a set range of displayed phase values for each row of images in the figure. It is clear that the difference increases, specifically at the W site, with a higher density of defects.

Finally, SFig. 9 shows the IAM and DFT projected potentials and their differences for the same defect configurations as in SFig. 8. The same trend as in the SSB images is observed: with a higher defect density (left to right), the DFT potential is increasing at the W site next to the S vacancies, compared to the IAM potential. This demonstrates that the phases are directly related to the potentials and the changes in them are caused by bonding and charge transfer.

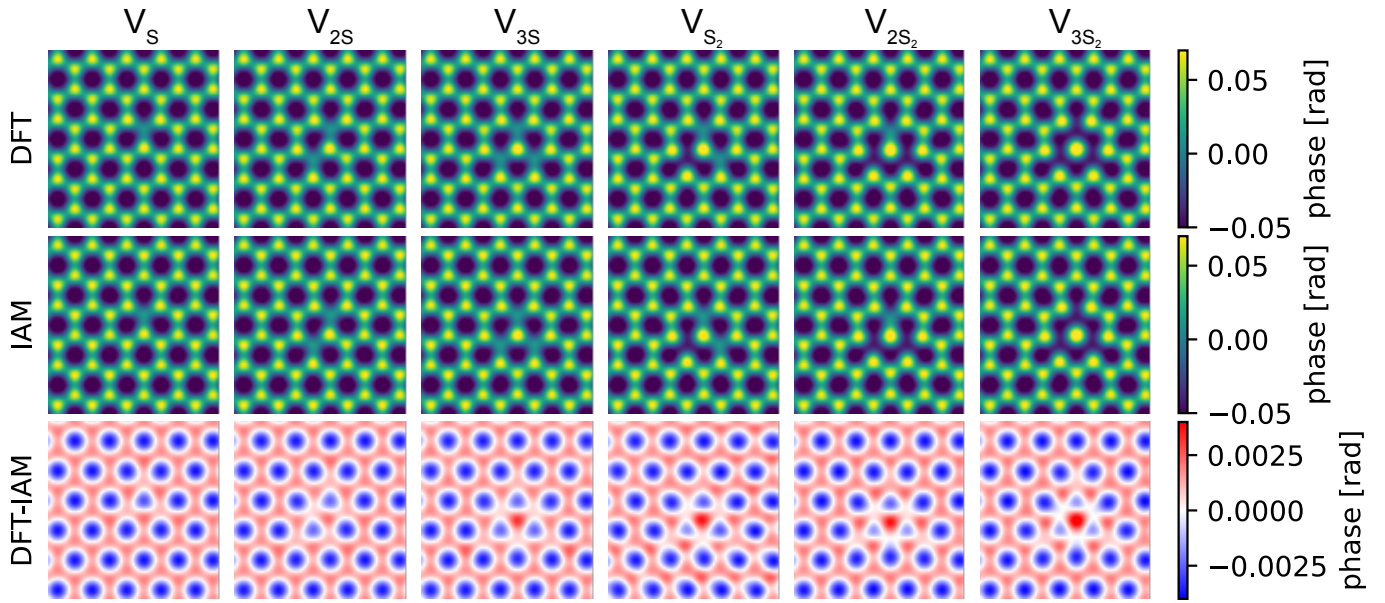
To elucidate the phase increase at the W site with increasing density of defects, we calculated the 3D pseudo valence electron density for the pristine WS_2 , the 3MV case, the 3DV case, and an isolated W atom. From the 3D volume, we calculated 2D electron density maps of a single slice of 0.07\AA thickness in top views and side views at the position of the W atom close to the defects. At this slice, the electron density of the S atoms are negligible in the top view. In all cases, the electron density of the 3DV configuration is lower, with the biggest difference in the side view. This is in agreement with the phase contrast we observe at different defect densities: the lower screening of the smaller electron density of W in the 3DV case leads to a higher phase.



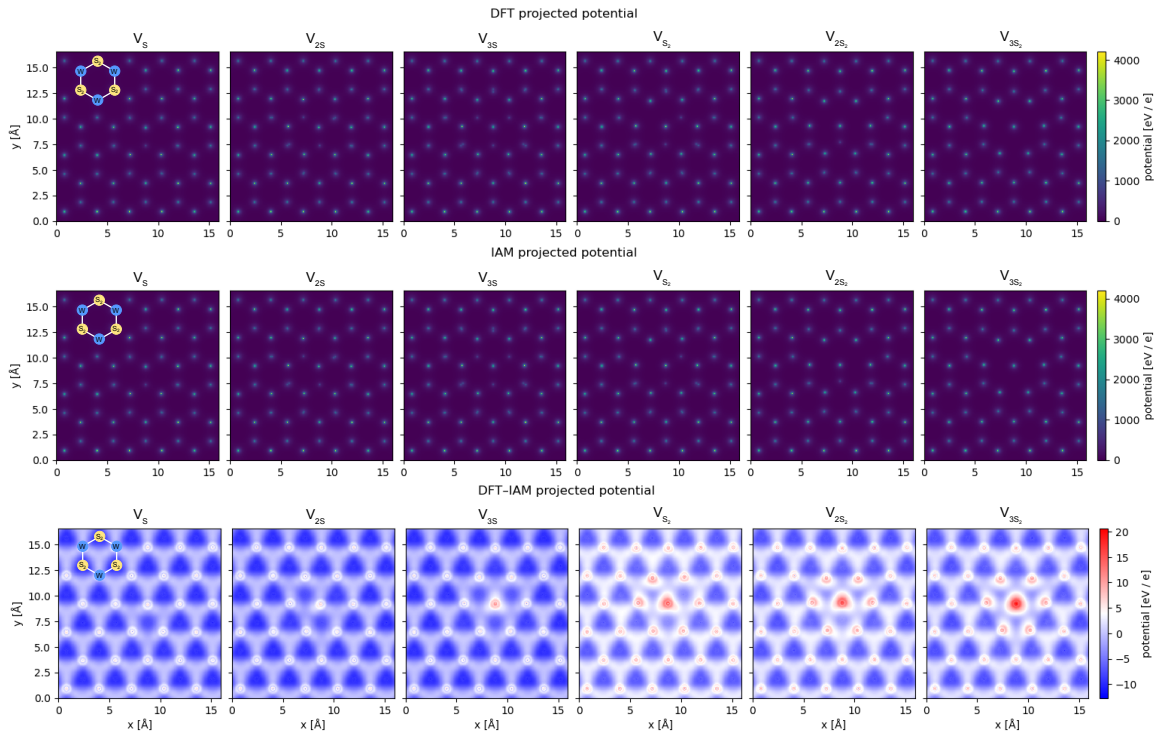
Supplemental Figure 6. **Experimental data from a defected region of WS_2 .** Regions of different vacancy configurations and defect densities are highlighted on the right. The green box shows a pristine region, the purple box mono vacancies and the blue box a region with divacancies. These atomic structure of the defect sites can be only identified in the SSB images.



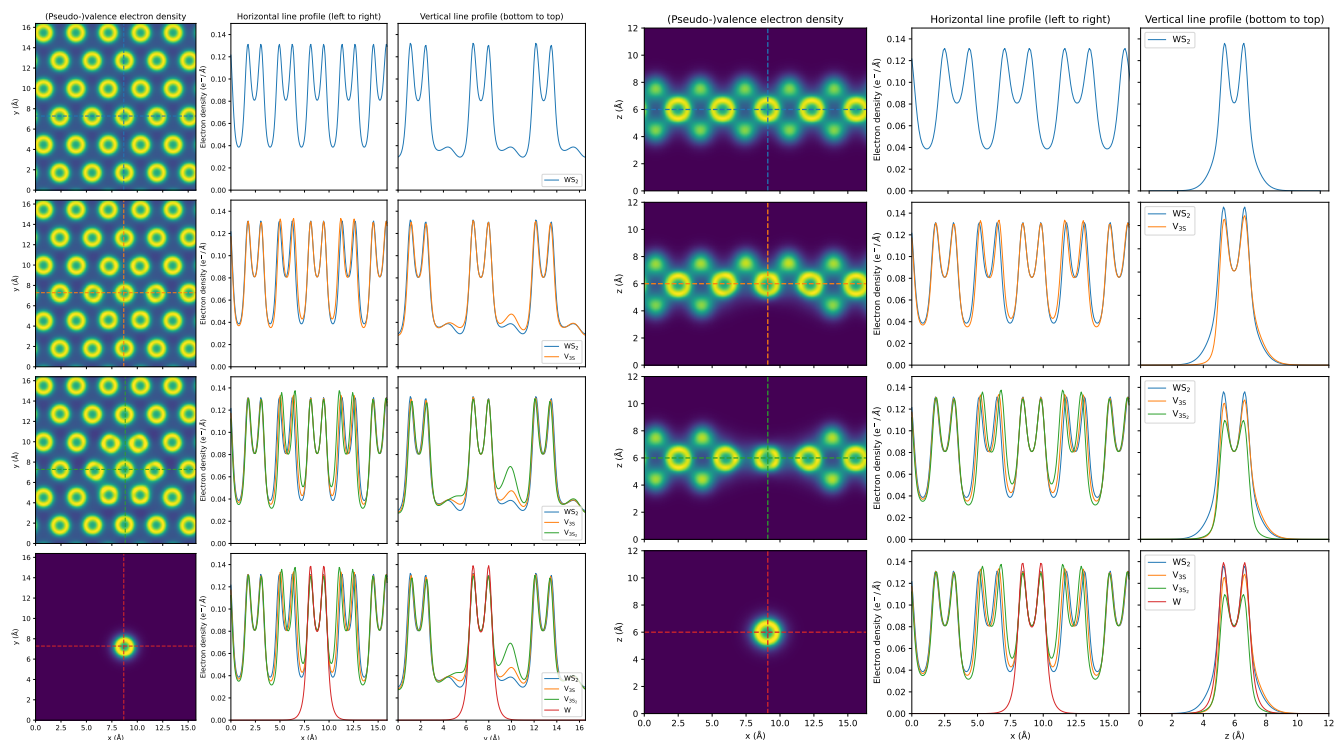
Supplemental Figure 7. **Analysis of phase cross sections at a defective area.** a) Simulated area that is analysed for Fig. 3c in the main manuscript. b) Experimental SSB image of a small defective area. c) Extracted phases of (b).



Supplemental Figure 8. **SSB ptychography images simulated based on DFT and IAM potentials and their difference for different vacancy configurations.** As the density of vacancies increases (left to right) more charge is transferred, resulting in greater contrast in the DFT-IAM image. The configurations correspond to a single monovacancy (MV), two MVs, three MVs, a single divacancy (DV), two DVs and three DVs.



Supplemental Figure 9. **Projected DFT and IAM potentials and their difference for the same vacancy configurations as shown in SFig. 8.** The density of defects (vacancies) increases left to right in the figure.



Supplemental Figure 10. **Pseudo valence electron density of (defective) WS_2 in top view (left) and side view (right).** From the 3D pseudo valence densities, the maps (first and third column) show a 2D slice (0.07 \AA thickness) at the height of the W atoms (second and fourth column). The density of defects is increased from top to bottom. The valence electron density is decreasing at the W site close to the defect, explaining the phase increase.